# Adsorbate coverage effects on the electroreduction of CO to acetate

Futian You [a,1], Ricardo Urrego-Ortiz [b,c,1], Steve Shao Wei Pan [a], Federico Calle-Vallejo [c,d,*], Boon Siang Yeo [a,**]

[a] *Department of Chemistry, National University of Singapore, 3 Science Drive 3, 117543, Singapore*
[b] *Department of Materials Science and Chemical Physics & Institute of Theoretical and Computational Chemistry (IQTCUB), University of Barcelona, C/ Martí i Franquès 1, Barcelona 08028, Spain*
[c] *Nano-Bio Spectroscopy Group and European Theoretical Spectroscopy Facility (ETSF), Department of Polymers and Advanced Materials: Physics, Chemistry and Technology, University of the Basque Country UPV/EHU, Av. Tolosa 72, San Sebastián 20018, Spain*
[d] *IKERBASQUE, Basque Foundation for Science, Plaza de Euskadi 5, Bilbao 48009, Spain*

A B S T R A C T

CO electroreduction (COR), powered by renewable electricity, shows promise for producing green chemicals at the industrial scale. Here, we aim to understand why amongst $C_2$ products, acetate is formed with relatively greater selectivity on Cu catalysts mounted in flow cells, as compared to in H-cells. We attribute this to improved CO transport in flow cells, which increases local pH and *CO coverage ($\theta_{*CO}$). The effect of local pH was verified through COR in different electrolytes, which shows a significant increase in the Faradaic efficiency ($FE$) of acetate as local pH rose. Higher CO concentrations in flow cells under similar local pH also substantially increased the $FE_{acetate}$, as compared to $FE_{ethylene}$ and $FE_{ethanol}$. This suggests that acetate formation is most sensitive to $\theta_{*CO}$. DFT calculations emphasize the importance of $\theta_{*CO}$ in favoring acetate formation from the *CHCO intermediate, and reveals the role of lateral interactions in the production of $C_2$ molecules.

## 1. Introduction

Electrocatalysis offers an appealing route for valorizing green electricity and $CO_2$ into valuable chemicals and fuels [1]. Among all $CO_2$ reduction ($CO_2$R) products, CO can be selectively produced on metal catalysts such as silver, gold and zinc [2–4]. The generated CO can then be further reduced on copper (Cu) into multi-carbon products such as ethylene, ethanol, acetate and *n*-propanol [5,6]. In recent years, there has been a growing interest in replacing $CO_2$ with CO for electro-reduction, as CO is a neutral gas and does not react with alkaline electrolytes to give (bi)carbonates [7]. However, CO solubility in water at 20 °C and 1 atm is only 1 mM [8]. Thus, severe CO mass-transport limitations are encountered when CO electroreduction (COR) is performed in traditional H-cells [5,9–13]. This has restricted the current density ($j$) of COR to ~1 mA cm$^{-2}$. To get a larger $j_{COR}$, flow cells equipped with gas diffusion electrodes (GDEs) have been widely adopted [6,14–16]. When COR was conducted on Cu catalysts in flow cells, the Faradaic efficiency ($FE$) of acetate surpassed 30 % and even reached 91 % [16–21]. Such

high selectivity for acetate is, in contrast, not commonly seen in H-cell studies of COR ($FE_{acetate} < 3$ %) [5,10–12,22], except for the work of Li et al.[9] and Wang et al. [13], which reported $FE_{acetate}$ of 61 and 56 %, respectively. More interestingly, the gaps in the $FE$s of ethylene (or ethanol) produced in H-cells and flow cells are not as large as those of acetate [5,10–12,16–22]. This suggests that $FE_{acetate}$ is more sensitive to cell configurations than $FE_{ethylene}$ and $FE_{ethanol}$. Given that the differences of catalysts, potentials, CO pressure and electrolytes, etc., used in these studies could also affect product selectivities, it is important to examine $FE_{acetate}$, $FE_{ethylene}$ and $FE_{ethanol}$ obtained in H-cells and flow cells under similar experimental conditions. Based on these results, we can then properly ascertain the underlying causes of the markedly higher sensitivity of $FE_{acetate}$ to cell configurations.

To explain the aforementioned gap between the $FE$s of acetate produced in H-cells and flow cells, we note that the major differences between these two cell configurations are: (i) local pH, which is affected by electrolytes, types of products formed, and current densities [20,23]; and (ii) mass transport of CO to the catalyst surface which can be

* Corresponding author at: Nano-Bio Spectroscopy Group and European Theoretical Spectroscopy Facility (ETSF), Department of Polymers and Advanced Materials: Physics, Chemistry and Technology, University of the Basque Country UPV/EHU, Av. Tolosa 72, San Sebastián 20018, Spain.
** Corresponding author.
*E-mail addresses:* federico.calle@ehu.es (F. Calle-Vallejo), chmyeos@nus.edu.sg (B.S. Yeo).
[1] These authors contributed equally to this work

described by *CO coverage ($\theta_{*CO}$); see Eq. (1) and Fig. 1a.

$$\theta_{*CO} = \theta_* \times p_{CO} \times e^{-\frac{\Delta G_{*CO}}{k_B T}} \qquad (1)$$

$\theta_*$ is the coverage of free surface sites, $p_{CO}$ is the CO partial pressure, $\Delta G_{*CO}$ is the CO adsorption energy on the surface (in eV), $k_B$ is the Boltzmann constant (in eV K$^{-1}$) and $T$ is the absolute temperature [24]. The two factors, i.e., local pH and $\theta_{*CO}$, have been shown to influence the formation of acetate during CO$_2$R and COR [17,20,25,26]. Local pH is important because it is generally accepted that acetate is produced by the reaction of a hydroxide anion (OH$^-$) with ethenone (CH$_2$CO) [9,17, 18,25,27]. $\theta_{*CO}$ is, in turn, important as it affects CH$_2$CO formation by promoting *CO dimerization and reducing C binding strength on the Cu surface [19,20,26].

With the above in mind, we provide in this work a rationale for how cell configurations influence CO reduction to acetate and insights into the effect of $\theta_{*CO}$ on C$_2$ selectivities. COR experiments were performed in 1 M KOH electrolyte using Cu catalysts thermally deposited on carbon paper. We first show that a flow cell delivers higher $FE_{acetate}$ compared to an H-cell (37 *vs.* 4 %). The larger average current density in the flow cell compared to that in the H-cell further indicates that the local pH and $\theta_{*CO}$ are presumably higher in the former than in the latter, both of which could increase $FE_{acetate}$. To assess the effect of local pH on $FE_{acetate}$, we reduced CO in a flow cell using 1 M KH$_2$PO$_4$, 0.5 M K$_2$HPO$_4$ and 1 M KOH electrolyte. We further studied the effect of $\theta_{*CO}$ on $FE_{acetate}$ under similar local pH values by reducing different concentrations of CO at –300 mA cm$^{-2}$. $FE_{acetate}$ was found to be most sensitive to $\theta_{*CO}$, as compared to $FE_{ethylene}$ and $FE_{ethanol}$. Co-electrolysis of $^{13}$CH$_2$I$_2$ and $^{12}$CO formed little $^{13}$CH$_3$$^{12}$COO$^-$, suggesting that an increased $\theta_{*CO}$ is unlikely to increase $FE_{acetate}$ via the coupling of *CH$_2$ and CO. Density functional theory (DFT) calculations show that high $\theta_{*CO}$ destabilizes the hydrogenation of *CHCO to *CHCHO, which is a key step for ethylene/ethanol production. In contrast, a high $\theta_{*CO}$ strengthens the formation of ethenone, which is an important precursor of acetate. In other words, a high $\theta_{*CO}$ enhances acetate production over ethylene and ethanol production.

## 2. Experimental

### 2.1. Preparation and characterization of thermally deposited Cu GDEs

An ~30 nm thick Cu (99.999 %, Kurt Lesker) film was thermally evaporated onto a carbon gas diffusion layer (GDL, Sigracet 38 BC) (Figure S1). The Cu layer was then coated with two carbon layers to increase its stability during electrolysis [28]. Specifically, a 3 cm × 4 cm Cu-deposited GDL was air-brushed with 12 mg carbon nanoparticles (Vulcan XC72) dispersed in an ink of 1.2 mL water (18.2 MΩ, Sartorius), 3.6 mL ethanol (≥ 99.8 %, VWR) and 12 µL Nafion 117 (5 wt.%, Sigma-Aldrich). It was then painted with an ink containing 72 mg graphite flakes (100 mesh, Ted Pella), 0.6 mL water, 0.6 mL ethanol and 24 µL Nafion 117. The electrode was dried using a hotplate heated at 60 °C, and will be referred to as Cu GDE.

The morphologies of the Cu surfaces before, during (represented by samples used for 30 min COR electrolysis) and after 1 h COR were characterized by scanning electron microscopy (SEM, JOEL JSM 6710 F; 1.91 × 10$^{-5}$ Pa; accelerating voltage of 20.0 kV; probe current of 8 pA; working distance of 6.4 mm; electrodes without carbon coatings were studied; Fig. 1b – c and S2). Energy-dispersive X-ray spectroscopy (EDS, JOEL JED-2300; 1.91 × 10$^{-5}$ Pa; accelerating voltage of 15.0 kV; probe current of 15 pA; working distance of 15 mm) was used to analyze the elements on the electrode surfaces (Fig. 1d and S3).

The surfaces of the Cu GDEs were characterized after their use for COR by cyclic voltammetry (CV) performed in N$_2$-saturated 1 M KOH in an H-cell (Fig. 1e). Before scanning CV, a potential of –1.03 V *vs.* standard hydrogen electrode (SHE) was applied for 5 min to remove residual oxygen. CV was scanned at 50 mV s$^{-1}$.
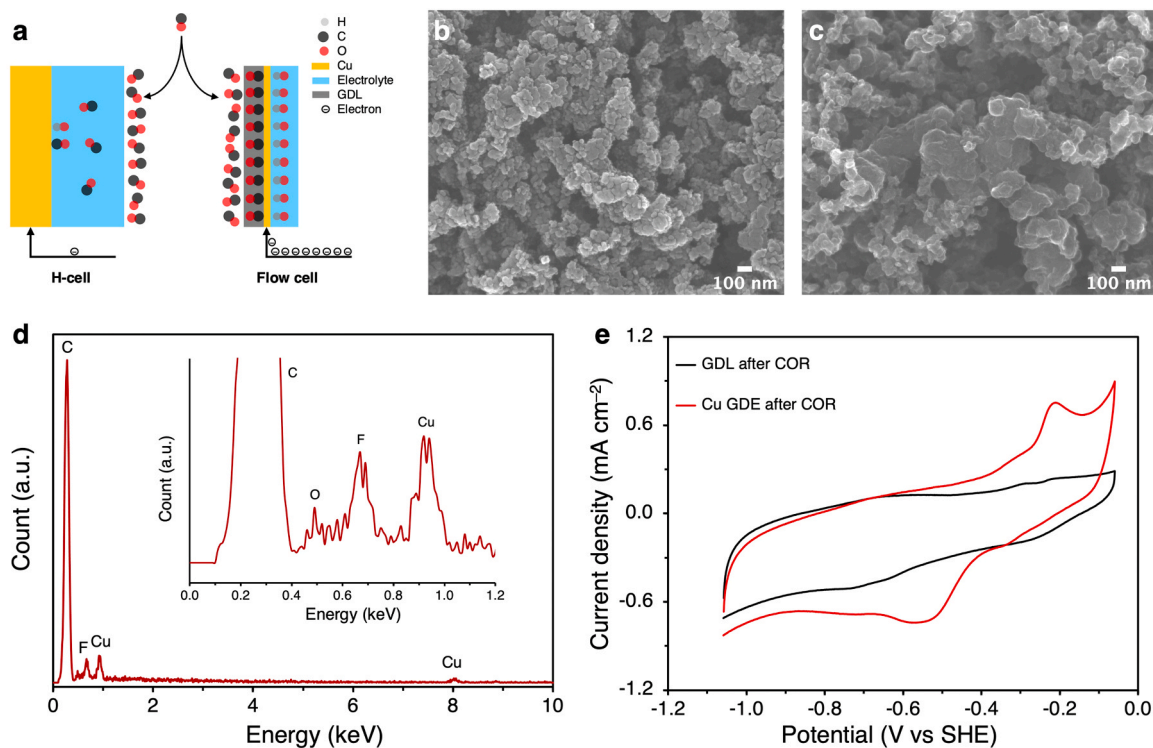
**Fig. 1.** (a) Comparison of CO electroreduction (COR) in H-cell and flow cell. Scanning electron microscopy images of Cu gas diffusion electrodes (Cu GDEs) (b) before, and (c) after their use for COR. (d) Energy-dispersive X-ray spectrum of as-prepared Cu GDE. The C and F signals originate from the carbon nanoparticles and polytetrafluoroethylene binder in the GDL. The O signal possibly originates from surface oxides on the Cu layer. (e) Cyclic voltammetry of carbon GDL and Cu GDE after COR. Cu GDEs without carbon coatings were characterized. COR was performed at –1.58 V in 1 M KOH electrolyte for 1 h.

## 2.2. Electrolysis

An H-cell and a flow cell custom-made using polyvinylidene difluoride (PVDF) were employed (Figures S4 – S5). The anodic and cathodic compartments of each cell were separated by an anion exchange membrane (AMV, AGC Asahi Glass). CO (99.97 %, Linde) was introduced into both cells at 5 SCCM using mass flow controllers (MFCs, Alicat, MC-100SCCM-D/5 M). The H-cell was equipped with a frit to improve CO transport to the catalyst. A flowmeter (Alicat, M-100SCCM-D/5 M) was used to measure the flow rate of gas exiting the cells.

In the H-cell, 1 M KOH (99.99 %, Sigma-Aldrich) was used as both catholyte (10 mL) and anolyte (8 mL). The reference electrode (RE) was Hg/HgO (1 M KOH, CHI) and the counter electrode (CE) was a graphite rod (OD 6 mm, Ted Pella). In the flow cell, 12 mL of catholyte was cycled by a peristaltic pump and separated from the 15 mL anolyte by an anion exchange membrane. Three types of electrolytes were used: 1 M KOH, 1 M potassium phosphate monobasic ($KH_2PO_4$, 99.8 %, Sigma-Aldrich) and 0.5 M potassium phosphate dibasic ($K_2HPO_4 \bullet 3 H_2O$, 99.8 %, Sigma-Aldrich). When 1 M KOH was used as the electrolyte, the RE was an Hg/HgO (1 M KOH, CHI), and the CE was a nickel foam (TMAX, diameter of 2 cm, thickness of 2 mm). When 1 M $KH_2PO_4$ or 0.5 M $K_2HPO_4$ was used as the electrolyte, the RE and CE were an Ag/AgCl (saturated KCl, Pine) and a graphite rod, respectively.

Cu GDEs of 1 cm in diameter (Figures S4c and S5c) were used for constant-potential electrolysis (Gamry Reference 600) in the H-cell and flow cell. The exposed geometric surface areas of GDE in the H-cell and flow cell were 0.38 and 0.20 cm$^2$, with diameters of 7 and 5 mm, respectively. Each electrolysis was performed for 1 h at different potentials with the *iR* drop compensated using the current interrupt mode. The working potentials were converted to potentials (V) *vs.* SHE according to Eqs. (2)–(3):

$$E_{SHE} = E_{Hg/HgO} + 0.098 \tag{2}$$

$$E_{SHE} = E_{Ag/AgCl} + 0.197 \tag{3}$$

For constant current electrolysis in the flow cell, the applied current density was fixed at –300 mA cm$^{-2}$ for 1 h in 1 M KOH. The CO concentration in the feed gas was adjusted by mixing it with $N_2$ (99.999 %, Chem-gas) with the total gas flow maintained at 5 SCCM.

The co-electrolysis of $^{13}$C-labelled diiodomethane ($^{13}CH_2I_2$, $\geq$ 98 atom% $^{13}$C, Sigma-Aldrich) and 10 vol.% CO was performed on Cu GDE at –300 mA cm$^{-2}$ for 1 h in 1 M KOH. 0.5 SCCM CO and 4.5 SCCM $N_2$ were first mixed and then bubbled into the $^{13}CH_2I_2$ liquid to transfer the $^{13}CH_2I_2$ vapor into the flow cell for electrolysis. For $^{13}CH_2I_2$ electrolysis, 5 SCCM $N_2$ was used as feed gas instead, while maintaining the other conditions. Each electrolysis experiment was repeated three times.

## 2.3. Quantification of products

COR gaseous products were quantified during electrolysis by a gas chromatograph (GC, Agilent 7890 A) equipped with two flammable ionization detectors (FID) and a thermal conduction detector (TCD) (Figure S6a–b). For each electrochemical measurement, five injections were obtained at an interval of 830 s, but only the last four were used for the quantitative analysis of products. The catholytes and anolytes were analyzed for acetate (Figure S6c) using a high-performance liquid chromatograph (HPLC, Agilent 1260 Infinity), with a variable wavelength detector. Electrolytes of 1 M KOH were neutralized and diluted ten-fold using 0.06 M sulfuric acid ($H_2SO_4$, 98 wt.%, Fisher Chemical) before HPLC analysis. Electrolytes of 1 M $KH_2PO_4$ and 0.5 M $K_2HPO_4$ were diluted ten-fold using ultrapure water before HPLC analysis. The catholytes were also analyzed by a headspace gas chromatograph with an FID (Headspace GC, Agilent 7890B and 7697 A) (Figure S6d).

## 2.4. Local pH modelling

The local pH within the boundary layer during COR was modeled according to the method introduced by Ma et al. in a flow cell [20] with details provided in Section S1.6 of the Supporting Information. The boundary layer between the electrode surface and the bulk electrolyte is a thin film where a pH gradient exists. The boundary layer thickness was determined using Eq. (4) by measuring the diffusion-limited current of ferricyanide reduction [20,29]:

$$\delta = \frac{D_{Fe(CN)_6^{3-}} \times c_{Fe(CN)_6^{3-}} \times F}{j} \tag{4}$$

$\delta$ is the boundary layer thickness; $D_{Fe(CN)_6^{3-}}$ is the diffusion coefficient of $Fe(CN)_6^{3-}$, $7.26 \times 10^{-6}$ cm$^2$ s$^{-1}$ [30]; $c_{Fe(CN)_6^{3-}}$ is the concentration of $Fe(CN)_6^{3-}$; $F$ is the Faraday constant, 96,485 C mol$^{-1}$ [31]; $j$ is the current density of ferricyanide reduction.

10 mM potassium ferricyanide ($K_3Fe(CN)_6$, 99.98 %, Sigma-Aldrich) was dissolved in 1 M $KH_2PO_4$, 0.5 M $K_2HPO_4$ and 1 M KOH, and reduced on a carbon GDL in the flow cell using the same procedures as COR except that 5 SCCM $N_2$ were used as feed gas (Figure S7). A carbon GDL (Sigracet 38 BC) was used as the inert electrode instead of Cu GDE so as to avoid reducing ferricyanide via galvanic exchange with Cu without electrolysis, as ferricyanide is an oxidant [20]. After the boundary layer thickness in each electrolyte was determined, local pH was modelled based on it (Figures S8 – S9).

## 2.5. Nuclear magnetic resonance spectroscopic analysis

1-D $^1$H nuclear magnetic resonance (NMR) spectra with water suppression were recorded on a Bruker Avance III HD 500 MHz mounted with a 5 mm BBO Prodigy (at 20 °C). Phenol (7.2 ppm, 99.1 %, VWR) and dimethylsulfoxide (2.6 ppm, Analytical Reagent, QRec) dissolved in $D_2O$ (4.8 ppm, 99.9 %, Cambridge Isotope Laboratories) were used as internal standards. For the 1-D $^1$H NMR analysis, one pulse experiment was pre-saturated on the water resonance with a $\pi/2$ pulse of 12 μs, and a recycle delay of 5 s was implemented while co-adding 256 scans per experiment.

## 2.6. Gas chromatography-mass spectrometry analysis

Gas samples from the co-electrolysis of $^{13}CH_2I_2$ and CO were analyzed using gas chromatography-mass spectrometry (GC-MS, Agilent 7890A-5975 C). The GC was equipped with a capillary column (HP-AL/S, Agilent) to separate the hydrocarbons. Manual injections with volumes of 250 μL at a split ratio of 1:500 were performed for gas samples. The GC temperature was held at 50 °C for 2 min, then ramped to 180 °C at 30 °C min$^{-1}$, and held at 180 °C for 19 min. The scanned mass range was 10 – 100 amu at positive polarity. $^{13}CH_4$ (99 atom%, Cambridge Isotopes) was mixed with $^{12}CH_4$ (99.99 vol%, Chem-gas) at different volume ratios to analyze the ion intensities at *m/z* of 15 and 17 (Figure S10a – b). A calibration curve (Figure S10c) was established on the ion ratio of $^{13}CH_4^+$ ($R_{ion}$) over the volume ratio of $^{13}CH_4$ in methane. $R_{ion}$ was calculated by Eq. (5):

$$R_{ion} = \frac{I_{m/z=17}}{I_{m/z=15} + I_{m/z=17}} \tag{5}$$

$I_{m/z=15}$ and $I_{m/z=17}$ are the intensity of signals at *m/z* of 15 and 17, respectively. These intensities were baseline corrected, before they were used for further analysis.

## 2.7. DFT calculations

DFT calculations were performed using the PBE exchange-correlation functional [32] and the VASP code using the projector augmented wave (PAW) method to describe ion-electron interactions

[33,34]. Cu surfaces were modelled using (4 × 4) slabs with four atomic layers each. The calculated lattice constant of Cu was 3.64 Å, typical of the PBE functional. The relaxations of the atoms were carried out using the conjugate gradient algorithm as implemented in VASP. For the relaxation of the slabs, the two top layers and the adsorbates were allowed to move, while the bottom layers were kept at the PBE-optimized bulk distances. The free atoms were allowed to relax until all the forces between the atoms were below 0.05 eV/Å (0.01 eV/Å for the molecules). A plane-wave energy cutoff of 450 eV was used in all calculations. The Fermi level was smeared using the Methfessel-Paxton method [35] with $k_B T = 0.2$ eV for the slab calculations, and 0.001 eV for the free molecules, and all energies were extrapolated to 0 K. The reciprocal space was sampled using Monkhorst-Pack meshes [36] of (3 × 3 × 1) for the slabs, and only the Γ-point for the gas-phase compounds. All calculations were spin restricted. Further details are provided in the Section S3 of the Supporting Information.

## 3. Results and discussion

### 3.1. Characterization of Cu GDEs

The as-prepared Cu GDE contained < 100 nm sized Cu particles, which agglomerated after 1 h COR (Fig. 1b – d). The Cu layer after COR showed redox peaks at –0.53 and –0.22 V *vs.* SHE in its cyclic voltammogram (Fig. 1e), which coincides with that of polycrystalline Cu [37]. All potentials hereafter are referenced to SHE to better compare the selectivities of $C_2$ products across different electrolytes. This is because the formation rates of $C_2$ products are dependent on potentials referenced to SHE [5,38,39].

### 3.2. COR on Cu GDEs using an H-cell and a flow cell

We first illustrate the effect of cell configurations on $C_2$ selectivities by comparing the COR performances in an H-cell and a flow cell. The electrodes, electrolytes and CO flow rates at atmospheric pressure and room temperature (23 °C) were kept the same in both cells. Constant-potential COR was carried out on Cu GDEs in 1 M KOH for 1 h to establish the distributions of the COR products (Tables S1–S4). To minimize the Cannizzaro disproportionation of acetaldehyde [40] (selectively formed at –1.0 V on rough Cu electrodes [13]) to acetate and ethanol, potentials were applied from –1.43 to –1.68 V.

When CO was reduced in the H-cell, ethylene was the most selectively formed $C_2$ product, with the highest $FE$ of 8.4 % at –1.53 V (Fig. 2a). Acetate was not detected until the potential became more negative than –1.48 V and achieved its highest $FE$ of 4.2 % at –1.53 V. Ethanol was detected at all potentials, with the highest $FE$ of 2.3 % at –1.48 V. Methane evolved at –1.48 V and reached its highest $FE$ of 4.2 % at –1.58 V, but this increasing trend was interrupted by a slight drop at –1.63 V, indicating a CO mass-transport limit. It is noteworthy that $FE_{ethylene}$ was higher than $FE_{acetate}$ at all potentials, which agrees with the work by Wang et al. [5]. In the region of potentials where acetate was detected, the $FE$ of acetate was higher than that of ethanol.

For COR performed in the flow-cell, the selectivity trends of all major $C_2$ products contrast with that of $H_2$ (Fig. 2b). While $FE_{H2}$ decreased in the range of –1.43 to –1.58 V, reaching a minimum of 11 % at –1.58 V, $FE_{acetate}$, $FE_{ethylene}$, and $FE_{ethanol}$ reached their highest values of 37 % at –1.58 V, 29 % at –1.53 V, and 8.4 % at –1.58 V, respectively (Table S3). The average current density ($j_{average}$) also increased, for example, from –46 (in the H-cell) to –296 (in the flow-cell) mA cm$^{-2}$ at –1.58 V (Tables S2 and S4). We note that among the $C_2$ products, acetate and ethylene were always more selectively produced than ethanol over the investigated potential region. More specifically, ethylene was the most selectively produced $C_2$ species at –1.43 and –1.48 V, while acetate was the most selectively produced $C_2$ species from –1.53 to –1.68 V. These results are in line with the COR work of Jouny et al., which reported that the $FE_{acetate}$ can surpass $FE_{ethylene}$ and $FE_{ethanol}$ at –1.43 V, where ethylene

and ethanol were both selectively produced [6]. Overall, these results show that a flow cell can deliver a markedly higher $FE_{acetate}$ than that in an H-cell under the analyzed conditions (37 *vs.* 4.2 %, which represents a 9× change). Such sensitivity to cell configurations was, in contrast, less observed for $FE_{ethylene}$ (29 *vs.* 8.4 %, which represents a 3× change) and $FE_{ethanol}$ (8.4 *vs.* 2.3 %, which represents a 4× change).

To assess the effect of local pH on the selectivities of $C_2$ products, we created different local pH values for COR in the flow cell by changing the electrolyte from 1 M KOH (bulk pH 13.9) to 1 M $KH_2PO_4$ (bulk pH 4.1) and 0.5 M $K_2HPO_4$ (bulk pH 9.1). We first observed that the formation rates of $C_2$ products from COR in three electrolytes are dependent on the potentials referenced to SHE (Tables S3 – S8), which corroborates with existing studies [5,38,39]. As a result, the selectivities of $C_2$ products mainly distribute over a potential range centered at around –1.6 V *vs.* SHE (Fig. 2b – d). More importantly, the $FE_{ethylene}$, $FE_{acetate}$ and $FE_{ethanol}$ increased alongside the bulk pH of the electrolyte, with the increment of $FE_{acetate}$ being the most significant (Fig. 2b – d). To exemplify the effect of local pH on the selectivities of $C_2$ products, we simulated the local pH during COR in 1 M $KH_2PO_4$, 0.5 M $K_2HPO_4$ and 1 M KOH at a representative potential of –1.58 or –1.59 V, where $FE_{acetate}$ was the highest in all three electrolytes (Figures S7 – S8). As the local pH near the electrode increased from 12.5 (in 1 M $KH_2PO_4$,) to 13.2 (in 0.5 M $K_2HPO_4$) and 14.0 (in 1 M KOH), $FE_{acetate}$ increased from 18 to 25 and 37 %, respectively (Fig. 2e). Interestingly, such a significant effect of local pH was not observed on the other $C_2$ products: $FE_{ethylene}$ only increased from 20 to 23 and 28 %, respectively, whereas $FE_{ethanol}$ increased from 5.2 to 6.4 and 8.4 %, respectively. This indicates that a high local pH improves the selectivity of acetate more significantly than that of ethylene and ethanol. We therefore conclude that similar local pH environments should be maintained when investigating other factors on acetate selectivity.

To understand the effect of $\theta_{*CO}$ on product formation while minimizing interferences due to local pH changes, we performed constant-current electrolysis in the flow cell with different CO concentrations. The $j_{average}$ of 1 h electrolysis was –296 mA cm$^{-2}$ at –1.58 V where acetate was most selectively produced. Therefore, a similar $j$ of –300 mA cm$^{-2}$ was applied to the same catalyst using the same electrolyte and electrolysis time to study the effect of $\theta_{*CO}$. Increasing the CO concentration led to an increase of $FE_{COR}$ and decrease of $FE_{H2}$ (Fig. 2f), pointing to a higher $\theta_{*CO}$. We note that the morphologies of the Cu catalysts throughout 1 h electrolyses were similar, regardless of the concentrations of the CO feed (Figure S2). As the CO concentration increased from 10 to 100 vol.%, the $FEs$ of acetate, ethylene and ethanol increased to different extents: $FE_{acetate}$ increased the most (from 1.6 to 35 %), followed by $FE_{ethylene}$ (from 3.2 to 24 %) and $FE_{ethanol}$ (from 1.0 to 5.8 %) (Fig. 2g and Tables S9 – S10). The trend is clearer after normalizing the $FEs$ of the products measured at different CO concentrations with respect to those measured at 10 vol.% CO: When CO concentration increased from 10 to 100 vol.%, the $FE_{acetate}$ increased by 21 folds, while the $FE_{ethylene}$ and $FE_{ethanol}$ only increased by 7 and 5 folds, respectively. This indicates that the selectivity of acetate is more sensitive to $\theta_{*CO}$, as compared to that of ethylene and ethanol. We also modeled the local pH during the constant-current electrolysis of 10 – 100 vol.% CO concentrations (Fig. 2h and S9) noting that, as the CO concentration increases, more $CH_2CO$ intermediates are formed that react with OH$^-$ to give acetate, which slightly decreases the local pH. Nonetheless, the local pH values obtained during the electrolysis for the different CO concentrations are still close to each other, with values between 14.0 – 14.1. Hence, increasing $\theta_{*CO}$ could affect factors other than local pH to promote acetate selectivity. Such an effect on promoting acetate selectivity is also much greater than that of promoting the selectivities of ethylene and ethanol.

### 3.3. Co-electrolysis of CO and $^{13}CH_2I_2$ on Cu GDEs

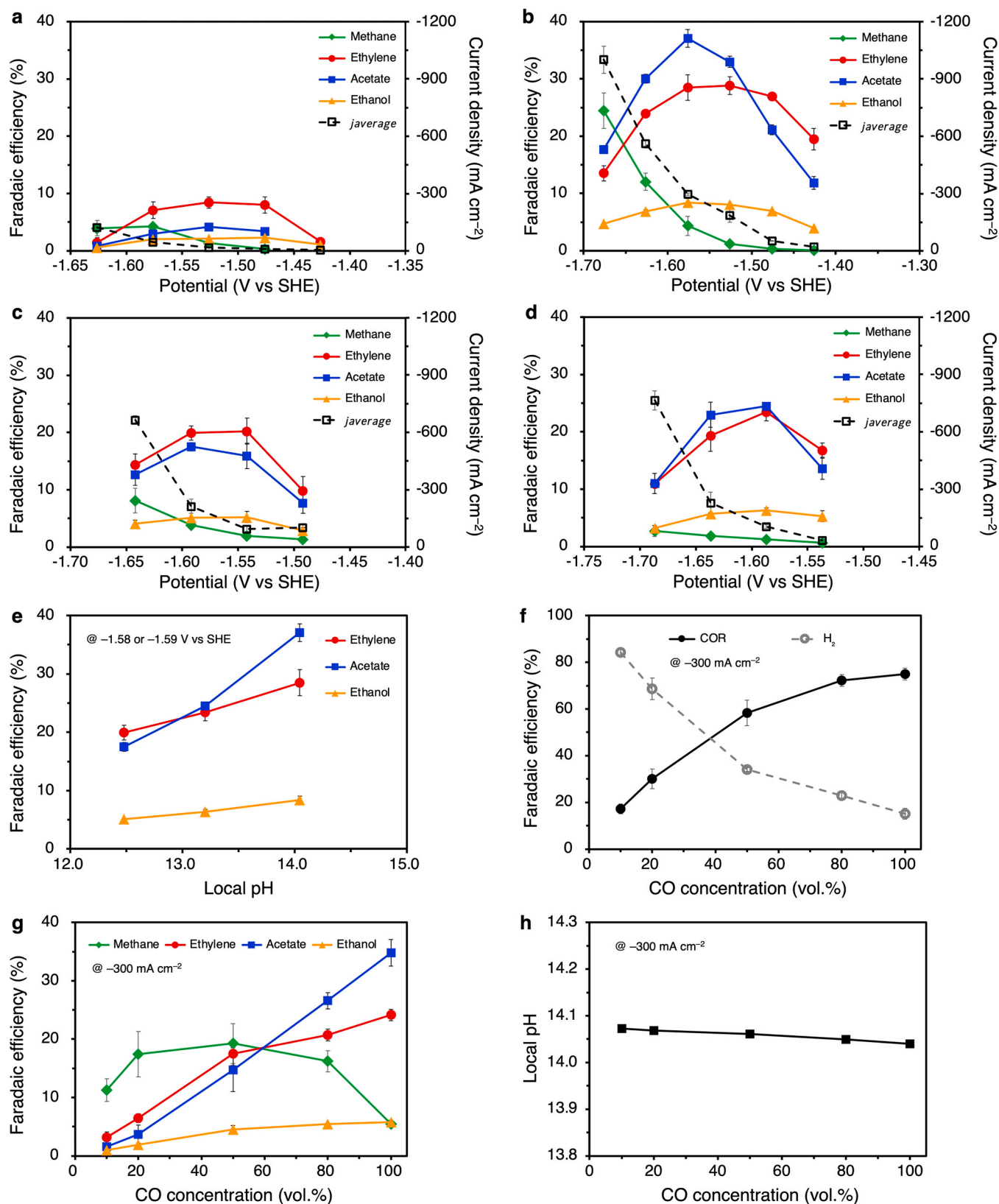The C-C coupling step that leads to the formation of ethylene and

**Fig. 2.** Faradaic efficiencies (*FEs*) of major products and the average current density (*j_average*) during 1 h COR on Cu GDEs at different potentials in (a) H-cell and 1 M KOH electrolyte, (b) flow cell and 1 M KOH electrolyte, (c) flow cell and 1 M KH$_2$PO$_4$ electrolyte, and (d) flow cell and 0.5 M K$_2$HPO$_4$ electrolyte. (e) *FEs* of C$_2$ products during 1 h COR in flow cell at –1.58 or –1.59 V under different local pH conditions. (f) *FEs* of all COR products and H$_2$, (g) *FEs* of major COR products, and (h) simulated local pH during 1 h electrolysis of different CO concentrations on Cu GDEs in a flow cell at –300 mA cm$^{-2}$. 1 M KOH electrolyte was used.

ethanol is widely accepted to be the dimerization of *CO [11,17,41–45]. Several studies have also proposed that the C-C backbone of acetate is formed by *CO dimerization, although others have hypothesized that it can be produced by asymmetric C-C coupling involving $CO_{(g)}$ and *CH$_2$ [46]. Looking at Fig. 2g, we find that as the CO concentration increases, $FE_{methane}$ first increases and then decreases. $FE_{methane}$ first increases because COR is facilitated by a higher $\theta_{*CO}$. There are two possible explanations for the decrease of $FE_{methane}$: (i) More *CH$_2$ species (precursor to CH$_4$) are consumed through coupling with CO (either gaseous or adsorbed) into CH$_2$CO, thus increasing acetate formation while decreasing methane formation; (ii) The dominating *CO dimerization under high $\theta_{*CO}$ suppresses the formation of *CH$_x$ species as previous studies have shown that it is energetically more favorable to hydrogenate a *CO dimer than a monomer [47].

To assess the possibility of the C-C backbone of acetate being formed by the reaction of *CH$_2$ with CO, we strategize to generate *$^{13}$CH$_2$ from $^{13}$C-labelled diiodomethane ($^{13}$CH$_2$I$_2$). Since diiodomethane is a water-insoluble liquid, spiking it into the aqueous electrolyte is inefficient for its electrolysis. Thus, we transferred $^{13}$CH$_2$I$_2$ vapor into the flow cell using a N$_2$ feed gas, and then electrolyzed it at –300 mA cm$^{-2}$. $^{13}$CH$_2$I$_2$ electrolysis generated no acetate but produced methane at a rate of 24 μmol cm$^{-2}$ h$^{-1}$ (Fig. 3a – b).

To minimize interferences from the naturally-occurring $^{13}$CH$_3$COO$^-$ from the COR (~1 % of all acetate ions produced according to the natural abundance of $^{13}$C [31]), we co-electrolyzed $^{13}$CH$_2$I$_2$ with only 10 vol.% CO (Table S11). When $^{13}$CH$_2$I$_2$ was flowed into the reactor by 10 vol.% CO, the acetate formation rate increased from 45 to 73 μmol cm$^{-2}$ h$^{-1}$ (Fig. 3a). However, nuclear magnetic resonance (NMR) analysis showed that the $^{13}$CH$_3$COO$^-$ ions were still at their natural abundance (Fig. 3c), which indicates that $^{13}$CH$_2$I$_2$ did not participate in the

formation of the $^{13}$CH$_3$COO$^-$. The increased acetate (including $^{12}$CH$_3$COO$^-$ and $^{13}$CH$_3$COO$^-$) formation rate could possibly be attributed to iodine species at the surface of the electrodes (Figure S3), which are known to promote C-C coupling [27,48–50].

On the other hand, the methane formation rate increased from 210 to 228 μmol cm$^{-2}$ h$^{-1}$ (Fig. 3b). Gas chromatography-mass spectrometry (GC-MS) results showed that *$^{13}$CH$_2$ moieties were introduced into the flow cell by $^{13}$CH$_2$I$_2$ as the mass spectrum of the methane peak displays its signal at $m/z$ of 17, which represent $^{13}$CH$_4^+$ from $^{13}$CH$_4$ (Fig. 3d). $^{13}$CH$_4$ corresponded to nearly 9.6 % of all methane molecules produced in the co-electrolysis of CO and $^{13}$CH$_2$I$_2$ (Fig. 3d and S10).

Overall, the above results suggest that the added *$^{13}$CH$_2$ was mostly converted to methane. Hence, we consider it unlikely that the increased CO concentration facilitates *CH$_2$ coupling with gaseous or adsorbed CO to form acetate. Instead, the significant effect of CO concentration or surface coverage on acetate formation should be attributed to its effect on the hydrogenation of key C$_2$ intermediates formed after *CO dimerization.

### 3.4. Hydrogenation of *CO dimers to CH$_2$CO$_{(g)}$

Our experiments show that CO reduces to acetate more selectively in a flow cell than in an H-cell. Since the high $\theta_{*CO}$ is not likely to promote acetate formation by opening an alternative *CH$_2$ + CO pathway, we now investigate whether it affects the hydrogenation of C$_2$ intermediates after the C-C coupling step. The formation of the C-C bond on Cu electrodes is generally believed to occur by *CO dimerization [11,41,44,45], which produces a bidentate adsorbate, as shown in Eq. (6):
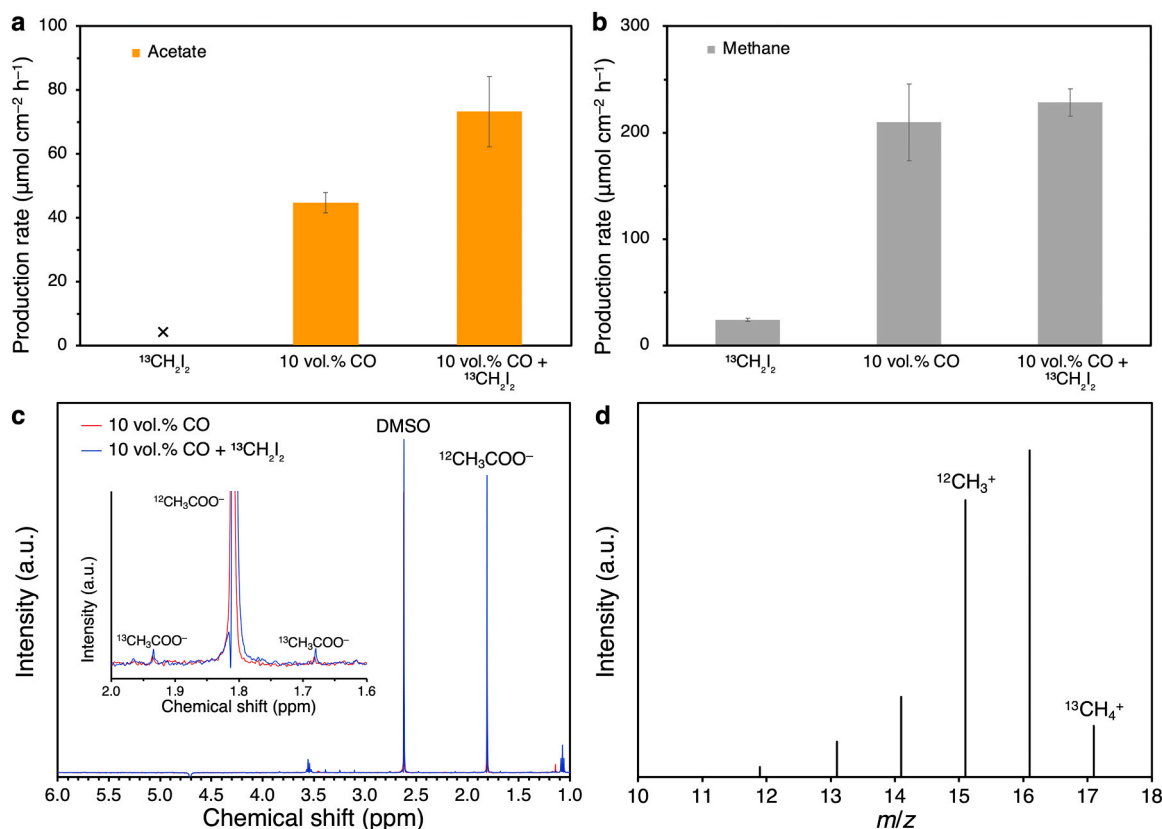
$$2*CO + e^- \rightarrow *C_2O_2^-* \qquad (6)$$



**Fig. 3.** Formation rates of (a) acetate and (b) methane in the 1 h electrolysis of $^{13}$CH$_2$I$_2$, 10 vol.% CO, and 10 vol.% CO and $^{13}$CH$_2$I$_2$ on Cu GDEs at –300 mA cm$^{-2}$ ('×' indicates not detected). (c) $^1$H NMR spectra of catholyte sampled after 1 h electrolysis of 10 vol.% CO and 1 h co-electrolysis of 10 vol.% CO and $^{13}$CH$_2$I$_2$ on Cu GDEs at –300 mA cm$^{-2}$. Dimethyl sulfoxide (DMSO) is used as internal standard. Inset in (c) is the enlarged spectra of acetate peaks. (d) Mass spectrum of gas products sampled from 1 h co-electrolysis of 10 vol.% CO and $^{13}$CH$_2$I$_2$ on Cu GDEs at –300 mA cm$^{-2}$.

An increased CO concentration should lead to a larger $\theta_{*CO}$, which will in turn promote *CO dimerization [51], facilitating the formation of $C_2$ products including ethylene, acetate, and ethanol. Since the increase in $FE_{acetate}$ observed in this work considerably exceeds that of $FE_{ethylene}$ and $FE_{ethanol}$ after increasing the CO concentration (Fig. 2g), the $\theta_{*CO}$ effect may not be merely attributed to promoting *CO dimerization, and the pathway from the *CO dimer to acetate ought to be investigated. Previous works revealed that ethylene and ethanol are formed on Cu via the hydrogenation of *CHCO into the oxametallacycle intermediate *CHCHO [41,45]. Such an intermediate is more stable than $CH_2CO_{(g)}$, the widely accepted precursor of acetate [9,17,18,25,27]. Here, we argue that $\theta_{*CO}$ influences the bifurcation of *CHCO into *CHCHO or $CH_2CO_{(g)}$ (Fig. 4). Alternatively, we note that Li et al. have previously proposed that the oxygenate-delivering reaction pathway of *CHCOH to *CHCHOH is favored under high $\theta_{*CO}$ [24]. They further showed that there is a positive correlation between $\theta_{*CO}$ and $FE_{acetate}$, but, interestingly, not between $\theta_{*CO}$ and $FE_{ethanol}$. In fact, their measured trend of $FE_{ethanol}$ over increasing $\theta_{*CO}$ is more similar to that of $FE_{ethylene}$ [24]. This contradiction of different $FE$ trends between the two oxygenates, i.e., ethanol and acetate, could be resolved if the hydrogenation of *CHCO branches into $CH_2CO_{(g)}$ and *CHCHO, the former producing acetate and the latter producing ethylene/ethanol.

### 3.5. Computational modelling

To evaluate the effect of $\theta_{*CO}$ on the reduction of *CHCO to *CHCHO or $CH_2CO_{(g)}$ and its facet dependence on Cu, we used DFT to calculate the energies of these bifurcating pathways on the prototypical Cu(111) and Cu(100) surfaces (the CO reduction pathways of which are relatively well-established) [41,47,52–54] at three different $\theta_{*CO}$: no *CO present (zero $\theta_{*CO}$), one co-adsorbed *CO (low $\theta_{*CO}$), and *CO fully surrounding the adsorbates (high $\theta_{*CO}$). The results are shown in Fig. 5 by means of free-energy diagrams. Details of the calculations and the related adsorption energies are given in Section S3 and Tables S12 – S13, respectively. The converged geometries of *CHCO and *CHCHO on Cu (111) are presented in Figure S13, and the respective structures of *CHCO, *CHCHO, and *CH₂CO for various $\theta_{*CO}$ on Cu(100) are shown in Figure S14. We have also accounted for hydrogen co-adsorption by assessing the effect of mixed coverages of *H and *CO on the electrocatalytic reduction of *CHCO to *CHCHO or $CH_2CO_{(g)}$ (Section S3). The observations and conclusions of those calculations are in line with those exposed herein.

We present first the results for Cu(111). In Fig. 5a, $CH_2CO_{(g)}$ is shown instead of *CH₂CO, as the chemical potential of the former in the gas phase is more negative than that of the latter in the adsorbed state at all

$\theta_{*CO}$ on this surface. Fig. 5a also shows that the free energies of *CHCO and *CHCHO are virtually the same in the zero- and low-coverage regimes, as can be noted from the small differences between the green and orange steps. From the zero- to low-coverage regimes, the adsorption of *CHCO and *CHCHO are weakened by 0.04 and 0.02 eV, respectively. In contrast, in the high-coverage regime, the adsorption energies of *CHCO and *CHCHO are sizably weakened by the repulsive interactions (i.e., lateral interactions) between them and *CO. Specifically, the weakening of *CHCO and *CHCHO on Cu(111) from low $\theta_{*CO}$ to high $\theta_{*CO}$ amounts to 0.10 and 0.14 eV respectively.

Furthermore, the free energies of *CHCHO on Cu(111) for zero and low $\theta_{*CO}$ are similar to that of $CH_2CO_{(g)}$ (corresponding to small energy differences of 0.01 and 0.03 eV, respectively; inset of Fig. 5a). However, at a high $\theta_{*CO}$, the free energy of *CHCHO is weakened such that $CH_2CO_{(g)}$ is more favorable by 0.18 eV. Indeed, as shown in the inset of Fig. 5a, this implies that a high $\theta_{*CO}$ weakens *CHCHO adsorption by no less than 0.15 eV, as compared to zero and low $\theta_{*CO}$.

The results of Cu(100) are presented in Fig. 5b, where the free energies of *CH₂CO are now depicted at zero and low $\theta_{*CO}$, as under these conditions, *CH₂CO is more stable than $CH_2CO_{(g)}$. Analogous to Cu (111), the free energies of the adsorbed species remain practically unchanged in the low-coverage condition for Cu(100) compared to the zero-coverage condition: *CHCO is weakened by 0.01 eV, and *CHCHO and *CH₂CO are strengthened by 0.02 eV. Only a high $\theta_{*CO}$ induces a substantial change, as *CHCO and *CHCHO are weakened by 0.24 and 0.36 eV as $\theta_{*CO}$ increases (from the zero- to the high-coverage condition). Contrary to the zero and low $\theta_{*CO}$, $CH_2CO_{(g)}$ is more stable than *CH₂CO by 0.09 eV at high $\theta_{*CO}$ (i.e., the free energy of *CH₂CO is –0.03 eV, not shown in Fig. 5). Importantly, on both Cu facets, high $\theta_{*CO}$ tends to destabilize *CHCHO to a greater extent compared to *CHCO and *CH₂CO, such that the reduction to $CH_2CO_{(g)}$ is favored.

The aforementioned energy shifts on Cu(100) at zero and low $\theta_{*CO}$ caused a more favorable reduction of *CHCO to *CHCHO, as compared to the reduction to *CH₂CO by 0.18 – 0.19 eV (vertical arrows in Fig. 5b). However, at high $\theta_{*CO}$ the two pathways of *CHCO to *CHCHO and $CH_2CO_{(g)}$ are comparable. The inset in Fig. 5b illustrates the effect of $\theta_{*CO}$ on the stability of *CHCHO on Cu(100): For zero and low $\theta_{*CO}$, *CHCHO is more stable than $CH_2CO_{(g)}$ by about 0.35 eV, but lateral interactions with *CO in the high-coverage regime destabilize *CHCHO such that it lies above $CH_2CO_{(g)}$ by 0.02 eV.

All in all, Fig. 5 shows that a high $\theta_{*CO}$ promotes the formation of $CH_2CO_{(g)}$ over *CHCHO. While the reduction of the latter leads to the $C_2$ products ethylene, acetaldehyde, and ethanol [41,55], acetate is formed from $CH_2CO_{(g)}$ in a pathway opened at a high $\theta_{*CO}$.

Our experiments and DFT calculations have shown that the high



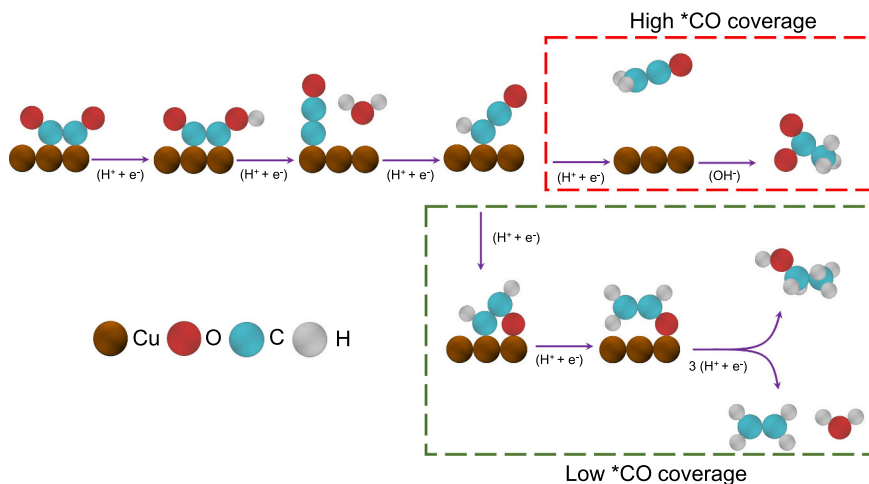**Fig. 4.** Proposed hydrogenation pathways of the *CO dimer to acetate ($CH_3COO^-$), ethylene ($CH_2CH_2$) and ethanol ($CH_3CH_2OH$) on Cu under different *CO coverage regimes. Brown, red, cyan, and white spheres represent Cu, O, C, and H atoms, respectively.

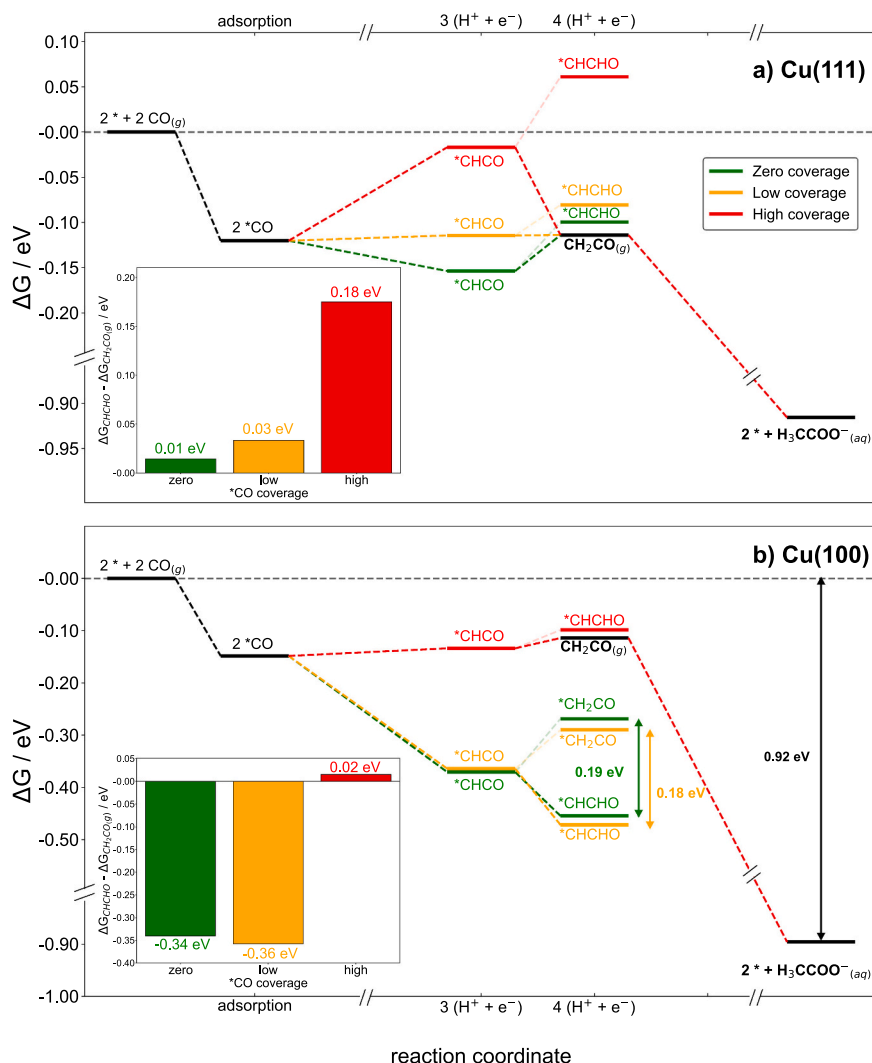**Fig. 5.** Condensed free-energy diagrams for the reduction of $CO_{(g)}$ to acetate at different $\theta_{*CO}$ on (a) Cu(111) and (b) Cu(100). The pathways of zero, low and high $\theta_{*CO}$, are shown in green, orange and red, respectively. In the low-coverage regime, one *CO is co-adsorbed. In the high-coverage regime, the adsorbates are fully surrounded by *CO (the structures are shown in Figure S13 for Cu(111) and Figure S14 for Cu(100)). For the green and orange pathways on Cu(100), *CHCHO is the main product of *CHCO hydrogenation. In the high-coverage regime, the production of $CH_2CO_{(g)}$ is preferred. On Cu(111), $CH_2CO_{(g)}$ production competes with *CHCHO even at zero and low $\theta_{*CO}$, but $CH_2CO_{(g)}$ is substantially favored by increasing $\theta_{*CO}$. Insets: thermodynamic indication of selectivity using the free energy difference of *CHCHO and $CH_2CO_{(g)}$. A positive value in the insets indicates that $CH_2CO_{(g)}$ is preferred over *CHCHO.

selectivity of acetate in the flow cell is caused by both high local pH and $\theta_{*CO}$, and pinpointed the effect of $\theta_{*CO}$ on the hydrogenation of the *CHCO intermediate towards acetate. We have also gained insights on the formation pathways of major $C_2$ products on Cu surfaces during COR: Our DFT calculations support the notion that ethylene and ethanol are formed via the *CHCHO intermediate, while acetate is formed via the $CH_2CO_{(g)}$ intermediate, the production of which is favored upon the *CHCHO destabilization by *CO repulsive lateral interactions. These results help understand different cell performances based on their architecture, and provide guidance to tuning product selectivities during COR.

## 4. Conclusion

We have shown that COR in a flow cell delivers a higher $FE_{acetate}$ than COR in an H-cell, which could be attributed to the higher local pH and $\theta_{*CO}$ in the flow cell. Increasing the local pH from 12.5 to 13.2 and 14.0 in the flow cell promoted $FE_{acetate}$ from 18 to 25 and 37 %, respectively. Increasing $\theta_{*CO}$ promoted $FE_{acetate}$ much more significantly than $FE_{ethylene}$ and $FE_{ethanol}$: When CO was enriched from 10 to 100 vol% in a flow cell

under −300 mA cm$^{-2}$, $FE_{acetate}$ increased by 33 percentage points (or by a factor of 21), while $FE_{ethylene}$ and $FE_{ethanol}$ increased by 21 and 5 percentage points (or by a factor of 7 and 5), respectively. Isotopic labelling experiments using $^{13}CH_2I_2$ as co-reactant in COR gave little $^{13}C$-labeled acetate, which ruled out the possibility that a higher $\theta_{*CO}$ contributes to acetate formation through increasing the *$CH_2$ coverage to couple with CO into ethenone, the precursor of acetate. Hence, apart from promoting *CO dimerization, the increased $\theta_{*CO}$ is most likely to affect acetate formation via hydrogenation of *CO dimers into ethenone. By means of DFT calculations, we corroborated the hypothesis that a higher $\theta_{*CO}$ favors the production of ethenone. This is done by destabilizing the formation of *CHCHO, which leads to ethylene and ethanol, with respect to $CH_2CO_{(g)}$ via repulsive lateral interactions. In broader terms, this work illustrates that the selectivity toward a target product during electrosynthesis can be steered by tuning the concentrations of feedstocks. Further insights could also be gained by looking at the different product distributions between $CO_2R$ and COR: Although local pH is regarded as an important factor for the higher acetate selectivity in COR compared to $CO_2R$ [56], it is also important to consider the effect of $\theta_{*CO}$ in the formation of $C_2$ products.

## CRediT authorship contribution statement

**Boon Siang Yeo:** Conceptualization, Data curation, Funding acquisition, Methodology, Project administration, Resources, Supervision, Writing – original draft, Writing – review & editing. **Federico Calle-Vallejo:** Data curation, Investigation, Supervision, Validation, Visualization, Writing – original draft, Writing – review & editing. **Steve Shao Wei Pan:** Investigation, Writing – review & editing. **Ricardo Urrego-Ortiz:** Formal analysis, Investigation, Visualization, Writing – original draft, Writing – review & editing. **Futian You:** Conceptualization, Data curation, Formal analysis, Investigation, Methodology, Validation, Visualization, Writing – original draft, Writing – review & editing.

## Declaration of Competing Interest

The corresponding author of this article (Boon Siang Yeo) is also a guest editor of the special issue 'Celebrating 15-year Anniversary of Singapore Catalysis Society (SCS)'.

https://www.sciencedirect.com/journal/applied-catalysis-b-environment-and-energy/special-issue/102QWR03Q2D

If there are other authors, they declare that they have no known competing financial interests or personal relationships that could have appeared to influence the work reported in this paper.

## Data Availability

Data will be made available on request.

## Acknowledgments

## Supporting information

Details of the experimental and computational procedures are presented in the Supporting Information.

## Appendix A. Supporting information

Supplementary data associated with this article can be found in the online version at doi:10.1016/j.apcatb.2024.124008.

## References

[1] M. Jouny, W. Luc, F. Jiao, General techno-economic analysis of $CO_2$ electrolysis systems, Ind. Eng. Chem. Res. 57 (2018) 2165–2177, https://doi.org/10.1021/acs.iecr.7b03514.

[2] Y. Hori, H. Wakebe, T. Tsukamoto, O. Koga, Electrocatalytic process of CO selectivity in electrochemical reduction of $CO_2$ at metal electrodes in aqueous media, Electrochim. Acta 39 (1994) 1833–1839, https://doi.org/10.1016/0013-4686(94)85172-7.

[3] S. Nitopi, E. Bertheussen, S.B. Scott, X. Liu, A.K. Engstfeld, S. Horch, B. Seger, I.E. L. Stephens, K. Chan, C. Hahn, J.K. Nørskov, T.F. Jaramillo, I. Chorkendorff, Progress and perspectives of electrochemical $CO_2$ reduction on copper in aqueous electrolyte, Chem. Rev. 119 (2019) 7610–7672, https://doi.org/10.1021/acs.chemrev.8b00705.

[4] M.P.L. Kang, M.J. Kolb, F. Calle-Vallejo, B.S. Yeo, The role of undercoordinated sites on zinc electrodes for $CO_2$ reduction to CO, Adv. Funct. Mater. 32 (2022) 2111597, https://doi.org/10.1002/adfm.202111597.

[5] L. Wang, S.A. Nitopi, E. Bertheussen, M. Orazov, C.G. Morales-Guio, X. Liu, D. C. Higgins, K. Chan, J.K. Nørskov, C. Hahn, T.F. Jaramillo, Electrochemical carbon monoxide reduction on polycrystalline copper: effects of potential, pressure, and pH on selectivity toward multicarbon and oxygenated products, ACS Catal. 8 (2018) 7445–7454, https://doi.org/10.1021/acscatal.8b01200.

[6] M. Jouny, W. Luc, F. Jiao, High-rate electroreduction of carbon monoxide to multi-carbon products, Nat. Catal. 1 (2018) 748–755, https://doi.org/10.1038/s41929-018-0133-2.

[7] M. Jouny, G.S. Hutchings, F. Jiao, Carbon monoxide electroreduction as an emerging platform for carbon utilization, Nat. Catal. 2 (2019) 1062–1070, https://doi.org/10.1038/s41929-019-0388-2.

[8] D.A. Wiesenburg, N.L. Guinasso Jr., Equilibrium solubilities of methane, carbon monoxide, and hydrogen in water and sea water, J. Chem. Eng. Data 24 (1979) 356–360, https://doi.org/10.1021/je60083a006.

[9] C.W. Li, J. Ciston, M.W. Kanan, Electroreduction of carbon monoxide to liquid fuel on oxide-derived nanocrystalline copper, Nature 508 (2014) 504–507, https://doi.org/10.1038/nature13249.

[10] Y. Hori, A. Murata, R. Takahashi, S. Suzuki, Electroreduction of carbon monoxide to methane and ethylene at a copper electrode in aqueous solutions at ambient temperature and pressure, J. Am. Chem. Soc. 109 (1987) 5022–5023, https://doi.org/10.1021/ja00250a044.

[11] Y. Hori, R. Takahashi, Y. Yoshinami, A. Murata, Electrochemical reduction of CO at a copper electrode, J. Phys. Chem. B 101 (1997) 7075–7081, https://doi.org/10.1021/jp970284i.

[12] Y. Hori, A. Murata, R. Takahashi, S. Suzuki, Electrochemical reduction of carbon monoxide to hydrocarbons at various metal electrodes in aqueous solution, Chem. Lett. 16 (1987) 1665–1668, https://doi.org/10.1246/cl.1987.1665.

[13] L. Wang, S. Nitopi, A.B. Wong, J.L. Snider, A.C. Nielander, C.G. Morales-Guio, M. Orazov, D.C. Higgins, C. Hahn, T.F. Jaramillo, Electrochemically converting carbon monoxide to liquid fuels by directing selectivity with electrode surface area, Nat. Catal. 2 (2019) 702–708, https://doi.org/10.1038/s41929-019-0301-z.

[14] D.S. Ripatti, T.R. Veltman, M.W. Kanan, Carbon monoxide gas diffusion electrolysis that produces concentrated $C_2$ products with high single-pass conversion, Joule 3 (2019) 240–256, https://doi.org/10.1016/j.joule.2018.10.007.

[15] J. Li, A. Xu, F. Li, Z. Wang, C. Zou, C.M. Gabardo, Y. Wang, A. Ozden, Y. Xu, D. H. Nam, Y. Lum, J. Wicks, B. Chen, Z. Wang, J. Chen, Y. Wen, T. Zhuang, M. Luo, X. Du, T.K. Sham, B. Zhang, E.H. Sargent, D. Sinton, Enhanced multi-carbon alcohol electroproduction from CO via modulated hydrogen adsorption, Nat. Commun. 11 (2020) 3685, https://doi.org/10.1038/s41467-020-17499-5.

[16] Y. Ji, Z. Chen, R. Wei, C. Yang, Y. Wang, J. Xu, H. Zhang, A. Guan, J. Chen, T.-K. Sham, J. Luo, Y. Yang, X. Xu, G. Zheng, Selective CO-to-acetate electroreduction via intermediate adsorption tuning on ordered Cu–Pd sites, Nat. Catal. 5 (2022) 251–258, https://doi.org/10.1038/s41929-022-00757-8.

[17] W. Luc, X. Fu, J. Shi, J.-J. Lv, M. Jouny, B.H. Ko, Y. Xu, Q. Tu, X. Hu, J. Wu, Q. Yue, Y. Liu, F. Jiao, Y. Kang, Two-dimensional copper nanosheets for electrochemical reduction of carbon monoxide to acetate, Nat. Catal. 2 (2019) 423–430, https://doi.org/10.1038/s41929-019-0269-8.

[18] P. Zhu, C. Xia, C.Y. Liu, K. Jiang, G. Gao, X. Zhang, Y. Xia, Y. Lei, H.N. Alshareef, T. P. Senftle, H. Wang, Direct and continuous generation of pure acetic acid solutions via electrocatalytic carbon monoxide reduction, Proc. Natl. Acad. Sci. U. S. A. 118 (2021) e2010868118, https://doi.org/10.1073/pnas.2010868118.

[19] J. Jin, J. Wicks, Q. Min, J. Li, Y. Hu, J. Ma, Y. Wang, Z. Jiang, Y. Xu, R. Lu, G. Si, P. Papangelakis, M. Shakouri, Q. Xiao, P. Ou, X. Wang, Z. Chen, W. Zhang, K. Yu, J. Song, X. Jiang, P. Qiu, Y. Lou, D. Wu, Y. Mao, A. Ozden, C. Wang, B.Y. Xia, X. Hu, V.P. Dravid, Y.M. Yiu, T.K. Sham, Z. Wang, D. Sinton, L. Mai, E.H. Sargent, Y. Pang, Constrained $C_2$ adsorbate orientation enables CO-to-acetate electroreduction, Nature 617 (2023) 724–729, https://doi.org/10.1038/s41586-023-05918-8.

[20] M. Ma, W. Deng, A. Xu, D. Hochfilzer, Y. Qiao, K. Chan, I. Chorkendorff, B. Seger, Local reaction environment for selective electroreduction of carbon monoxide, Energy Environ. Sci. 15 (2022) 2470–2478, https://doi.org/10.1039/d1ee03838a.

[21] P. Wang, H. Yang, C. Tang, Y. Wu, Y. Zheng, T. Cheng, K. Davey, X. Huang, S. Z. Qiao, Boosting electrocatalytic $CO_2$-to-ethanol production via asymmetric C-C coupling, Nat. Commun. 13 (2022) 3754, https://doi.org/10.1038/s41467-022-31427-9.

[22] L. Wang, D.C. Higgins, Y. Ji, C.G. Morales-Guio, K. Chan, C. Hahn, T.F. Jaramillo, Selective Reduction of CO to Acetaldehyde with CuAg Electrocatalysts, Proc. Natl. Acad. Sci. U. S. A. 117 (2020) 12572–12575, https://doi.org/10.1073/pnas.1821683117.

[23] N. Gupta, M. Gattrell, B. MacDougall, Calculation for the cathode surface concentrations in the electrochemical reduction of $CO_2$ in $KHCO_3$ solutions, J. Appl. Electrochem. 36 (2005) 161–172, https://doi.org/10.1007/s10800-005-9058-y.

[24] J. Li, Z. Wang, C. McCallum, Y. Xu, F. Li, Y. Wang, C.M. Gabardo, C.-T. Dinh, T.-T. Zhuang, L. Wang, J.Y. Howe, Y. Ren, E.H. Sargent, D. Sinton, Constraining CO coverage on copper promotes high-efficiency ethylene electroproduction, Nat. Catal. 2 (2019) 1124–1131, https://doi.org/10.1038/s41929-019-0380-x.

[25] H.H. Heenen, H. Shin, G. Kastlunger, S. Overa, J.A. Gauthier, F. Jiao, K. Chan, The mechanism for acetate formation in electrochemical $CO_{(2)}$ reduction on Cu: selectivity with potential, pH, and nanostructuring, Energy Environ. Sci. 15 (2022) 3978–3990, https://doi.org/10.1039/d2ee01485h.

[26] J. Hou, X. Chang, J. Li, B. Xu, Q. Lu, Correlating CO coverage and CO electroreduction on Cu via high-pressure *in situ* spectroscopic and reactivity investigations, J. Am. Chem. Soc. 144 (2022) 22202–22211, https://doi.org/10.1021/jacs.2c09956.

[27] Y. Zhou, R. Ganganahalli, S. Verma, H.R. Tan, B.S. Yeo, Production of $C_3$-$C_6$ acetate esters via CO electroreduction in a membrane electrode assembly cell, Angew. Chem. Int. Ed. 61 (2022) e202202859, https://doi.org/10.1002/anie.202202859.

[28] C.-T. Dinh, T. Burdyny, M.G. Kibria, A. Seifitokaldani, C.M. Gabardo, F.P. García de Arquer, A. Kiani, J.P. Edwards, P. De Luna, O.S. Bushuyev, C. Zou, R. Quintero-Bermudez, Y. Pang, D. Sinton, E.H. Sargent, $CO_2$ electroreduction to ethylene via hydroxide-mediated copper catalysis at an abrupt interface, Science 360 (2018) 783–787, https://doi.org/10.1126/science.aas9100.

[29] E.L. Clark, J. Resasco, A. Landers, J. Lin, L.-T. Chung, A. Walton, C. Hahn, T. F. Jaramillo, A.T. Bell, Standards and protocols for data acquisition and reporting for studies of the electrochemical reduction of carbon dioxide, ACS Catal. 8 (2018) 6560–6570, https://doi.org/10.1021/acscatal.8b01340.

[30] S.J. Konopka, B. McDuffie, Diffusion coefficients of ferri- and ferrocyanide ions in aqueous media, using twin-electrode thin-layer electrochemistry, Anal. Chem. 42 (1970) 1741–1746, https://doi.org/10.1021/ac50160a042.

[31] W.M.L. Haynes, D. R, T.J. Bruno. CRC Handbook of Chemistry and Physics, 97th ed., CRC Press, Boca Raton, FL, 2016.

[32] J.P. Perdew, K. Burke, M. Ernzerhof, Generalized gradient approximation made simple, Phys. Rev. Lett. 77 (1996) 3865–3868, https://doi.org/10.1103/PhysRevLett.77.3865.

[33] G. Kresse, J. Furthmüller, Efficient iterative schemes for *ab initio* total-energy calculations using a plane-wave basis set, Phys. Rev. B 54 (1996) 11169–11186, https://doi.org/10.1103/PhysRevB.54.11169.

[34] G. Kresse, D. Joubert, From ultrasoft pseudopotentials to the projector augmented-wave method, Phys. Rev. B 59 (1999) 1758–1775, https://doi.org/10.1103/PhysRevB.59.1758.

[35] M. Methfessel, A.T. Paxton, High-precision sampling for Brillouin-zone integration in metals, Phys. Rev. B 40 (1989) 3616–3621, https://doi.org/10.1103/PhysRevB.40.3616.

[36] H.J. Monkhorst, J.D. Pack, Special points for Brillouin-zone integrations, Phys. Rev. B 13 (1976) 5188–5192, https://doi.org/10.1103/PhysRevB.13.5188.

[37] S. Fletcher, R.G. Barradas, J.D. Porter, The anodic oxidation of copper amalgam and polycrystalline copper electrodes in LiOH solution, J. Electrochem. Soc. 125 (1978) 1960–1968, https://doi.org/10.1149/1.2131336.

[38] J. Li, D. Wu, A.S. Malkani, X. Chang, M.J. Cheng, B. Xu, Q. Lu, Hydroxide is not a promoter of $C_{2+}$ product formation in the electrochemical reduction of CO on copper, Angew. Chem. Int. Ed. 59 (2020) 4464–4469, https://doi.org/10.1002/anie.201912412.

[39] J. Li, X. Chang, H. Zhang, A.S. Malkani, M.J. Cheng, B. Xu, Q. Lu, Electrokinetic and in situ spectroscopic investigations of CO electrochemical reduction on copper, Nat. Commun. 12 (2021) 3264, https://doi.org/10.1038/s41467-021-23582-2.

[40] Y.Y. Birdja, M.T.M. Koper, The importance of Cannizzaro-type reactions during electrocatalytic reduction of carbon dioxide, J. Am. Chem. Soc. 139 (2017) 2030–2034, https://doi.org/10.1021/jacs.6b12008.

[41] F. Calle-Vallejo, M.T.M. Koper, Theoretical considerations on the electroreduction of CO to $C_2$ species on Cu(100) electrodes, Angew. Chem. Int. Ed. 52 (2013) 7282–7285, https://doi.org/10.1002/anie.201301470.

[42] H.J. Peng, M.T. Tang, J. Halldin Stenlid, X. Liu, F. Abild-Pedersen, Trends in oxygenate/hydrocarbon selectivity for electrochemical $CO_{(2)}$ reduction to $C_2$ products, Nat. Commun. 13 (2022) 1399, https://doi.org/10.1038/s41467-022-29140-8.

[43] R. Dorakhan, I. Grigioni, B.-H. Lee, P. Ou, J. Abed, C. O'Brien, A. Sedighian Rasouli, M. Plodinec, R.K. Miao, E. Shirzadi, J. Wicks, S. Park, G. Lee, J. Zhang, D. Sinton, E.H. Sargent, A silver–copper oxide catalyst for acetate electrosynthesis from carbon monoxide, Nat. Synth. (2023) 448–457, https://doi.org/10.1038/s44160-023-00259-w.

[44] J.H. Montoya, C. Shi, K. Chan, J.K. Nørskov, Theoretical insights into a CO dimerization mechanism in $CO_2$ electroreduction, J. Phys. Chem. Lett. 6 (2015) 2032–2037, https://doi.org/10.1021/acs.jpclett.5b00722.

[45] O. Piqué, F. Viñes, F. Illas, F. Calle-Vallejo, Elucidating the structure of ethanol-producing active sites at oxide-derived Cu electrocatalysts, ACS Catal. 10 (2020) 10488–10494, https://doi.org/10.1021/acscatal.0c01880.

[46] Y. Wang, D. Wang, C.J. Dares, S.L. Marquard, M.V. Sheridan, T.J. Meyer, $CO_2$ reduction to acetate in mixtures of ultrasmall $(Cu)_n(Ag)_m$ bimetallic nanoparticles, Proc. Natl. Acad. Sci. U. S. A. 115 (2018) 278–283, https://doi.org/10.1073/pnas.1713962115.

[47] E. Pérez-Gallent, G. Marcandalli, M.C. Figueiredo, F. Calle-Vallejo, M.T.M. Koper, Structure- and potential-dependent cation effects on CO reduction at copper single-crystal electrodes, J. Am. Chem. Soc. 139 (2017) 16412–16419, https://doi.org/10.1021/jacs.7b10142.

[48] H. Li, T. Liu, P. Wei, L. Lin, D. Gao, G. Wang, X. Bao, High-rate $CO_2$ electroreduction to $C_{2+}$ products over a copper-copper iodide catalyst, Angew. Chem. Int. Ed. 60 (2021) 14329–14333, https://doi.org/10.1002/anie.202102657.

[49] T. Kim, G.T.R. Palmore, A scalable method for preparing Cu electrocatalysts that convert $CO_2$ into $C_{2+}$ products, Nat. Commun. 11 (2020) 3622, https://doi.org/10.1038/s41467-020-16998-9.

[50] A.S. Varela, W. Ju, T. Reier, P. Strasser, Tuning the catalytic activity and selectivity of Cu for $CO_2$ electroreduction in the presence of halides, ACS Catal. 6 (2016) 2136–2144, https://doi.org/10.1021/acscatal.5b02550.

[51] R.B. Sandberg, J.H. Montoya, K. Chan, J.K. Nørskov, CO-CO coupling on Cu facets: Coverage, strain and field effects, Surf. Sci. 654 (2016) 56–62, https://doi.org/10.1016/j.susc.2016.08.006.

[52] W. Luo, X. Nie, M.J. Janik, A. Asthagiri, Facet dependence of $CO_2$ reduction paths on Cu electrodes, ACS Catal. 6 (2015) 219–229, https://doi.org/10.1021/acscatal.5b01967.

[53] X. Nie, W. Luo, M.J. Janik, A. Asthagiri, Reaction mechanisms of $CO_2$ electroreduction on Cu(111) determined with density functional theory, J. Catal. 312 (2014) 108–122, https://doi.org/10.1016/j.jcat.2014.01.013.

[54] A. Rendón-Calle, S. Builes, F. Calle-Vallejo, A brief review of the computational modeling of $CO_2$ electroreduction on Cu electrodes, Curr. Opin. Electrochem. 9 (2018) 158–165, https://doi.org/10.1016/j.coelec.2018.03.012.

[55] K.J.P. Schouten, Y. Kwon, C.J.M. van der Ham, Z. Qin, M.T.M. Koper, A new mechanism for the selectivity to $C_1$ and $C_2$ species in the electrochemical reduction of carbon dioxide on copper electrodes, Chem. Sci. 2 (2011) 1902–1909, https://doi.org/10.1039/c1sc00277e.

[56] J.Y.T. Kim, C. Sellers, S. Hao, T.P. Senftle, H. Wang, Different distributions of multi-carbon products in $CO_2$ and CO electroreduction under practical reaction conditions, Nat. Catal. 6 (2023) 1115–1124, https://doi.org/10.1038/s41929-023-01082-4.